



Cite this: *Phys. Chem. Chem. Phys.*,
2017, **19**, 8815

Probe dependence on polar solvation dynamics from fs broadband fluorescence†

Tatu Kumpulainen, Arnulf Rosspeintner and Eric Vauthey*

Polar solvation dynamics of six 7-aminocoumarins and 4-aminophthalimide (**4AP**) are investigated using broadband Fluorescence UP-conversion Spectroscopy (FLUPS) combined with a global analysis based on time-dependent band-shape functions. The solvation dynamics of the coumarins in ethanol exhibit only minor differences but are, however, significantly different from that of **4AP**. The band-shape parameters, width and asymmetry, exhibit much larger variation even among the coumarins and are correlated with the amount of excess excitation energy. Differences in the solvation dynamics of **4AP** and a selected coumarin, **C151**, are also observed in dimethyl sulfoxide demonstrating the molecularity of solvation *i.e.* solvation depends on the solute and does not solely reflect the dynamic properties of the solvent. These differences are attributed to specific solute–solvent interactions due to hydrogen bonding. In a weakly interacting solvent, benzonitrile, the solvation dynamics of **4AP** and **C151** are nearly identical.

Received 1st February 2017,
Accepted 2nd March 2017

DOI: 10.1039/c7cp00706j

rsc.li/pccp

1 Introduction

Polar solvation dynamics play a key role in several condensed phase chemical reactions, especially those involving charged or dipolar species, such as electron-transfer^{1–9} and proton-transfer^{10–15} reactions.^{16–21} Interaction with the polar environment can alter the reaction barrier through different stabilization of the reactant, transition or product states thus directly influencing the reaction rate. Moreover, investigations of the solvation dynamics on complex chemical^{22–24} or biological^{25–31} environments can yield valuable information about the local dielectric surroundings that is otherwise difficult or even impossible to access. For all the above cases, detailed understanding of the solvation dynamics and their dependence on the probe and the solvent is of paramount importance.

Solvent dynamics can be investigated using several approaches such as dielectric dispersion, optical Kerr effect or photon-echo experiments.^{32–35} One of the most used approaches is, however, the time-dependent Stokes shift method.^{36–38} This method utilizes push–pull type fluorophores which exhibit a large difference in the permanent dipole moment between the ground and the excited states. Upon excitation of such molecules, the surrounding solvent begins to reorient to accommodate the new charge distribution in

order to minimize the overall free energy. During this process, the free energy separation of the ground and excited states is reduced resulting in the dynamic Stokes shift (frequency down-shift) of the fluorescence emission. The spectral response function, $C(t)$, a measure of the solvation free energy, is obtained from the time evolution of the fluorescence band position as:³⁹

$$C(t) = \frac{\tilde{\nu}(t) - \tilde{\nu}(\infty)}{\tilde{\nu}(0) - \tilde{\nu}(\infty)}, \quad (1)$$

where $\tilde{\nu}(0)$, $\tilde{\nu}(t)$, and $\tilde{\nu}(\infty)$ are the frequencies of the fluorescence band position at time 0, t , and ∞ , respectively.

The most common method to obtain the spectral response function is the spectral reconstruction method described by Maroncelli and Fleming.⁴⁰ It involves measuring single wavelength fluorescence decays (fs or ps) over a wavelength range and fitting them individually to multi-exponential functions. The decay integrals are then normalized to the corrected steady-state emission intensities at each wavelength in order to obtain the time-resolved emission spectra (TRES).⁴¹ Finally, the TRES are fitted with log-normal^{42,43} functions, eqn (2), at each time step to obtain the band-shape parameters. The fluorescence band positions used to construct $C(t)$ are determined either from the mean (first moment)⁴³ or the peak frequency.

However, this approach has several shortcomings. The first and the most obvious shortcoming is the small number of data points (often 10–15) used in the spectral analysis of the band-shape parameters. Secondly, the normalization procedure is sensitive to both the steady-state spectrum and the decay integral. The steady-state intensity is usually very low in the blue side of the spectrum and can yield relatively large errors.

Department of Physical Chemistry, University of Geneva, 30 Quai Ernest Ansermet, Geneva, Switzerland. E-mail: Eric.Vauthey@unige.ch; Fax: +41 22 379 65 18;

Tel: +41 22 379 65 37

† Electronic supplementary information (ESI) available: Additional spectra and fitting parameters of all compounds, anisotropy decays and estimation of the degree of specific solute–solvent interactions for **C151** and **4AP**. See DOI: 10.1039/c7cp00706j

Accurate decay integrals, on the other hand, require a proper description of the short-time (dependent on the instrument response function) and the long-time (not well resolved in fs measurements) behavior. The last problem arises from the estimation of the time-zero emission spectra, *i.e.* the spectra prior to any solvent relaxation, which is required to construct $C(t)$. Due to the ultrafast inertial components of solvation in polar solvents,^{44,45} the estimation of $\tilde{\nu}(0)$ from the time-resolved data can be difficult and subject to large errors. Therefore, $\tilde{\nu}(0)$ is often estimated independently with the help of steady-state measurements in nonpolar and polar solvents, for example.⁴⁶ All these aspects have been thoroughly discussed in the seminal paper by Maroncelli and coworkers on the solvation dynamics of coumarin 153.⁴⁷

Broadband FLuorescence UP-conversion Spectroscopy (FLUPS) has enabled more detailed investigations on solvation dynamics and is able to overcome some of the problems discussed above.^{48–50} The first major advantage is the density of points for the spectral fitting (usually more than an order of magnitude greater). Second, photometric calibration of the obtained data directly produces corrected intensities over the whole emission range rendering the normalization procedure unnecessary. In addition, the chirp caused by the group velocity dispersion (GVD) can be independently determined thus improving the accuracy of the spectra at short times.⁴⁹ However, the FLUPS data is usually analyzed in an analogous manner to the spectral reconstruction method *i.e.* the time traces are analyzed with the log-normal functions to obtain the band-shape parameters used to construct $C(t)$.

Despite the wealth of investigations on polar solvation dynamics, only a few systematic studies on the probe dependence appear in the literature.^{51–58} This is particularly important to test the linear response approximation,^{59,60} which states that solvent relaxation is independent of how far from equilibrium it starts. In other words, solvent relaxation should be independent of the probe, at least in the absence of specific solute–solvent interactions. Maroncelli and coworkers investigated the solvation dynamics of 16 different fluorescent probes in 1-propanol at 253 K using time-correlated single photon counting (TCSPC) with ~ 20 ps effective time resolution.⁵⁴ They found that simple aromatic amines exhibited two-fold faster solvation times compared to the other probes, which was attributed to specific hydrogen-bonding interactions with the former. In a more recent study, Ernstring and coworkers studied the solvation dynamics of four probes in water and five in methanol using broadband FLUPS with a 85 fs instrument response function (IRF).⁵⁷ The solvation dynamics were found to be nearly identical in water and could be also reproduced from the dielectric dispersion data using a simple continuum theory supporting the linear response approximation.⁶¹ On the other hand, significant differences were observed in methanol and attributed to rotational diffusion of the probe. The rotational movement could be accounted for by dividing the observed $C(t)$ by $[r(t)]^\alpha$ where $r(t)$ is the normalized fluorescence anisotropy decay of the solute and α is a solute-dependent empirical power coefficient. This produced the $C(t)$ of the “slowest” probe, which was considered to be immobile on the time scale of the solvation. Recently, a similar approach was

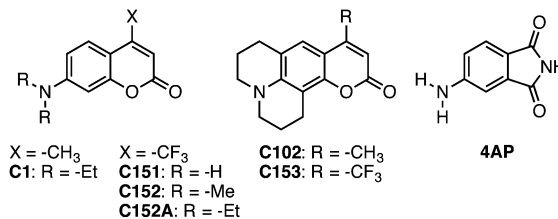


Chart 1 Structures of the solvation probes.

used to correlate the solvation dynamics of two probes in room temperature ionic liquids.⁵⁸

Our study aims to address two key issues of the previous studies on polar solvation dynamics. The first aim is to improve the data analysis by using a global model to directly obtain the time-dependent behavior of all the band-shape parameters from the FLUPS data. This has two main advantages over the conventional spectral fitting. First, the method enables direct analysis of the whole dataset from $t < 0$ with a reduced number of parameters and, similar to a recent algorithm for analysing transient absorption data,⁶² can account for the convolution with the IRF and the chirp due to the GVD. This greatly improves the fit at short times and, more importantly, directly yields the time-zero spectrum. Second, by using statistically meaningful weighting, we are able to judge the goodness of the fit using the χ_r^2 method. The model is described in detail in the Experimental section.

The second aim of the paper is to investigate the probe dependence and the effect of specific solute–solvent interactions on the solvation dynamics. To this end, we measured the solvation dynamics of seven push–pull probes (Chart 1), six 7-aminocoumarins (**C1**, **C102**, **C151**, **C152**, **C152A**, and **C153**) and 4-aminophthalimide (**4AP**), in ethanol and analyzed the broadband FLUPS data both with the spectral analysis and the global model. The differences of the two analysis methods are discussed. Additionally, a fixed excitation wavelength of 400 nm enables us to systematically investigate the effect of excess excitation energy. Last, we explore the effect of rotational diffusion of the solute on the solvation dynamics⁵⁷ of two structurally similar probes, **C151** and **4AP**, in three solvents, ethanol, benzonitrile and dimethyl sulfoxide.

2 Experimental section

2.1 Materials

All dyes were of laser grade (**BBOT** and **C153** from Radiant Dyes, others from Exciton) and used without further purification. **4AP** (Alfa Aesar) was recrystallized from methanol prior to use. Absolute ethanol (EtOH, +99.5%, Acros Organics), benzonitrile (PhCN, +99.9%, Sigma-Aldrich), dimethyl sulfoxide (DMSO, +99.9%, Alfa Aesar) and 2-methylbutane (2MB, +99%, Acros Organics) were used as received.

2.2 Spectroscopic measurements

Steady-state absorption spectra were recorded using a Varian Cary 50 spectrophotometer and emission spectra on a Horiba

Scientific FluoroMax-4 fluorimeter, corrected using a set of secondary emissive standards.⁶³ All steady-state and time-resolved measurements were performed at room temperature (22 ± 2 °C).

The ns time-correlated single photon counting setup⁶⁴ used to measure the fluorescence lifetimes and fs single wavelength fluorescence up-conversion setup^{65,66} used for the fluorescence anisotropies have been described in detail previously.

Broadband FLUPS measurements were performed on a setup similar to that described in detail in ref. 49 and 50. In brief, excitation was performed with ~ 100 fs pulses at 400 nm generated by frequency doubling part of the output of a standard 1 kHz Ti:Sapphire amplified system. The pump intensity on the sample was below 1 mJ cm^{-2} . The gate pulses at 1340 nm were produced by an optical parametric amplifier (TOPAS Prime, Light Conversion). Detection of the up-converted spectra was performed with a home-built spectrograph coupled to a CCD camera (Andor, DV420A-BU). The full width at half-maximum of the cross correlation of the gate with the solvent Raman signal was approximately 170 fs. Time-resolved emission spectra were recorded in two sequential measurements with a linear time grid from -2 to 2 ps and with a logarithmic time grid extending up to 1.2 ns. A typical measurement consisted of 15 successive scans with 1 s collection time at each time step. The raw data were transferred into spectra vs. wavenumber and subsequently corrected by calibration with secondary emissive standards as described in ref. 49. The chirp due to GVD was determined by measuring the instantaneous response of **BBOT** in all solvents used.

2.3 Data analysis methods

2.3.1 Spectral and global analysis. As explained in the introduction, the dynamic Stokes shift is most often analysed by spectral fitting using the log-normal function.^{42,43}

$$F(\tilde{\nu}) = I_0 \begin{cases} \exp[-\ln(2)\{\ln(1 + a(\tilde{\nu})/b)\}^2] & a(\tilde{\nu}) > -1 \\ 0 & a(\tilde{\nu}) \leq -1 \end{cases} \quad (2)$$

$$a(\tilde{\nu}) = \frac{2b(\tilde{\nu} - \tilde{\nu}_0)}{\Delta x} \quad (3)$$

where I_0 is the peak intensity at $t = 0$, b the asymmetry parameter, $\tilde{\nu}_0$ the peak position, and Δx the width parameter. The integral of the band, A , can be calculated according to eqn (4).

$$A = I_0 \frac{\Delta x}{2} \exp\left[\frac{b^2}{4 \ln 2}\right] \sqrt{\frac{\pi}{\ln 2}} \quad (4)$$

After the spectral analysis, the obtained parameters are fitted assuming multi-exponential (or sometimes stretched exponential) behavior.⁴⁷

In the global analysis, we have reversed the order. The parameters are first assumed to exhibit multi-exponential behavior in order to simulate their time dependence. To account for the finite duration of the excitation pulse, the multi-exponential function accounting for the time dependence of the fluorescence

band integral is convolved with a Gaussian-simulated IRF which has an analytical form:

$$A(t) = \sum_{i=1}^n \frac{\alpha_i}{2} \exp\left(-\frac{t-t_0}{\tau_i}\right) \exp\left(\frac{\sigma^2}{4\tau_i^2}\right) \left[1 + \operatorname{erf}\left(\frac{t-t_0 - \frac{\sigma^2}{2\tau_i}}{\sigma}\right)\right], \quad (5)$$

where α_i are the amplitudes associated with the lifetimes, τ_i , σ is the Gaussian width, and t_0 is the shift of the Gaussian. The other parameters are simulated according to:

$$X(t) = \begin{cases} \alpha_\infty + \sum_{i=1}^n \alpha_i \exp\left(-\frac{t-t_0}{\tau_i}\right) & t - t_0 \geq 0 \\ \alpha_\infty + \sum_{i=1}^n \alpha_i & t - t_0 < 0 \end{cases} \quad (6)$$

where $X(t)$ represents $b(t)$, $\tilde{\nu}_0(t)$, or $\Delta x(t)$, t_0 is the shift of the Gaussian obtained from eqn (5), and α_∞ is the amplitude at $t = \infty$.

Synthetic non-chirped time-resolved fluorescence spectra can be simulated by substituting the above equations into eqn (2). Optionally, one could apply the chirp correction to the data (as it is routinely done in spectral analysis) and use the above fitting functions. However, this is not optimal because the chirp correction generally involves interpolation and would alter the measured data values and the standard errors. Hence, it is more convenient to simulate the chirp in the fit function. In this case the interpolation can be performed on a smooth function using a very tight interpolation grid, contrary to the experimental data.

The chirp parameters were determined separately using a **BBOT** sample in the corresponding solvent⁴⁹ and fitting the decays at selected wavelengths with eqn (5). The obtained t_0 values were further analyzed with a chirp polynomial, eqn (7),⁶⁷ to account for the GVD throughout the detection window (the emission of **BBOT** only covers a part).

$$t_0(\tilde{\nu}) = p_1 + p_2 \tilde{\nu}^2 + p_3 \tilde{\nu}^4, \quad (7)$$

where p_1 , p_2 , and p_3 are the polynomial coefficients.

With the functions presented above, one can generate a synthetic dataset which is compared with the experimental data. The best fit is achieved through multiple iterations of nonlinear least-square optimization on a minimization function defined as:

$$f_{\min} = \sum \left(\frac{Y_{\text{fit}} - Y_{\text{data}}}{\text{SE}} \right)^2, \quad (8)$$

where Y_{fit} is the simulated and Y_{data} the measured dataset, and SE is the standard error of the data. The data is obtained from an average of N scans (usually 15) and the standard error from the corresponding standard deviation divided by \sqrt{N} . The goodness of the fit can be judged from the shape of the residual, eqn (8) at the optimized Y_{fit} , and from the χ_r^2 value.

To further optimize the robustness and usability of the global analysis, we implemented the conventional spectral fit into the algorithm prior to the global analysis (see Fig. 1).

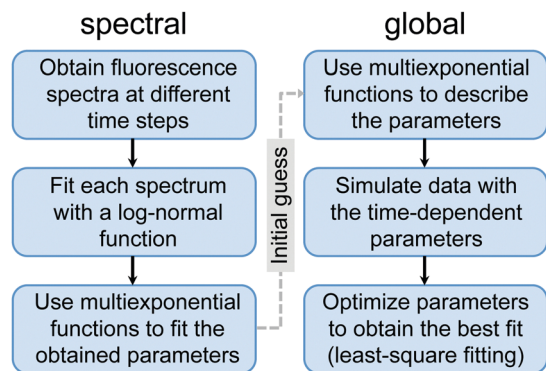


Fig. 1 Basic concept of the combined spectral and global analysis.

This serves two main purposes. First, this allows us to directly compare the results obtained from the two different approaches. Second, the parameters obtained from the spectral fit serve as a meaningful initial guess for the global analysis. This greatly speeds up the global analysis routine. Additionally, the obtained band-shape parameters at discrete time steps serve as an additional guide to the eye in judging the goodness of the fit.

2.3.2 Estimation of the time-zero spectra. The time-zero emission spectra in ethanol were estimated with the method described by Maroncelli and coworkers.^{46,47} In brief, absorption and emission spectra of each compound are measured in a nonpolar solvent (2-methylbutane) and used as intrinsic band-shape functions after conversion to the transition dipole moment representation.⁶⁸ The absorption in polar solvent is fitted with a convolution integral of the intrinsic band-shape function and a Gaussian with two adjustable parameters, the width and the shift of the Gaussian. These parameters represent the broadening and the solvatochromic shift, respectively, due to the polar environment. The determined Gaussian is then used to convolve the intrinsic emission band-shape function to obtain the final time-zero emission spectrum in polar solvent. Full details of the method are described in ref. 46. The band-shape parameters of the time-zero emission spectra were obtained from fits with the log-normal function, eqn (2).

2.3.3 Fluorescence anisotropy decays. Due to the long lifetime of 4AP in aprotic solvents and the high repetition rate of the laser (~ 80 MHz), the data showed extremely high background counts at $t < 0$. We had to account for this to obtain reliable fits and χ_r^2 estimations. Hence the anisotropy decays were estimated from:

$$r(t) = \frac{[I(t)_{\parallel} - \text{bg}_{\parallel}] - [I(t)_{\perp} - \text{bg}_{\perp}]}{[I(t)_{\parallel} - \text{bg}_{\parallel}] + 2[I(t)_{\perp} - \text{bg}_{\perp}]}, \quad (9)$$

where I and bg are the total fluorescence decay and the background (I at $t < 0$), respectively, measured at the parallel (\parallel) and the perpendicular (\perp) polarizations of the pump pulse relative to the gate pulse. The standard error was estimated through error propagation of the above equation according to:

$$\text{SE} = \sqrt{\left(\frac{\partial r}{\partial I_{\parallel}} \Delta I_{\parallel}\right)^2 + \left(\frac{\partial r}{\partial I_{\perp}} \Delta I_{\perp}\right)^2}, \quad (10)$$

where $\Delta I = \sqrt{I}$ are assumed to follow counting statistics and $\Delta \text{bg} = 0$. Weighted fits according to eqn (8) yielded meaningful χ_r^2 estimations and enabled discrimination between the different exponential models.

3 Results

3.1 Steady-state spectra

The steady-state absorption (gray) and emission (red) spectra of all compounds in EtOH are presented in Fig. 2. The emission spectra were fitted with log-normal functions to obtain the peak frequencies which are summarized in Table 1. The best fits are represented by the red solid lines in Fig. 2. The dashed vertical line indicates the fixed excitation wavelength and illustrates the increasing excess excitation energy in the series of coumarins.

3.2 Time-resolved broadband fluorescence

Time-resolved broadband fluorescence of all compounds was measured in EtOH. Representative spectra of C151 are presented in Fig. 3(a) together with the best global fit, (b), and weighted residual, (c). The estimated t_0 from the chirp polynomial is indicated by the dashed black line and the peak frequency by the dashed white line. The spectra, best global fits, and residuals of the other compounds are shown in Fig. S1 (ESI[†]).

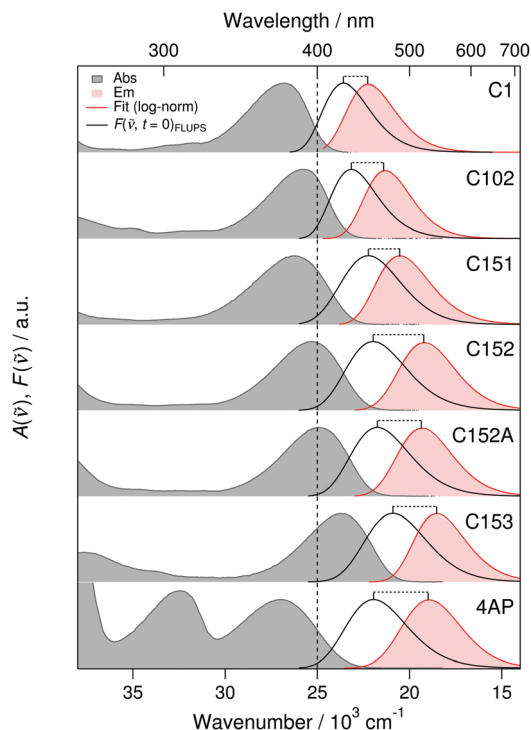


Fig. 2 Absorption (gray) and emission (red) spectra of the solvation probes in EtOH. The emission spectra were analyzed with log-normal functions (red line). The vertical dashed line shows the excitation wavelength used in all experiments in EtOH. The time-zero emission spectra obtained from the global analysis of the FLUPS data are indicated by the black solid lines. The dashed horizontal lines indicate the dynamic Stokes shift observed in the FLUPS measurements.

Table 1 Parameters of the time-zero and the relaxed emission spectra together with the parameters of the solvation dynamics in EtOH. All frequency parameters were obtained from fits of log-normal functions and are given in 10^3 cm^{-1}

Compound	Spectral properties ^a							Solvation dynamics ^b						
	$\tilde{\nu}_0^{\text{est}}$	$\tilde{\nu}_0^{\text{FLUPS}}$	$\tilde{\nu}_\infty^{\text{SS}}$	$\tilde{\nu}_\infty^{\text{FLUPS}}$	$\Delta\tilde{\nu}_{\text{est}}$	$\Delta\tilde{\nu}_{\text{obs}}$	$\Delta\tilde{\nu}_{\text{dif}}$	α_1	τ_1/ps	α_2	τ_2/ps	α_3	τ_3/ps	$\langle\tau\rangle/\text{ps}$
C1	23.94	23.59	22.20	22.27	1.74	1.32	-0.43	0.30	0.28	0.20	2.8	0.50	31.9	16.6
C102	23.03	23.16	21.29	21.41	1.73	1.75	0.01	0.25	0.30	0.20	3.3	0.56	35.5	20.4
C151	21.77	22.23	20.49	20.53	1.28	1.70	0.42	0.31	0.28	0.21	2.9	0.48	30.7	15.3
C152	21.81	21.98	19.17	19.24	2.64	2.73	0.10	0.26	0.32	0.24	2.9	0.50	29.4	15.4
C152A	21.65	21.75	19.29	19.36	2.36	2.39	0.03	0.26	0.37	0.23	3.1	0.51	30.6	16.6
C153	20.56	20.90	18.50	18.53	2.06	2.37	0.31	0.27	0.31	0.22	3.1	0.50	32.2	17.0
C153^c	20.70	20.58	18.62	18.63	2.08	1.95	-0.13	0.23	0.27	0.25	5.0	0.52	29.9	16.7
4AP	21.90	21.95	18.94	18.99	2.96	2.96	0.00	0.17	0.42	0.21	4.4	0.61	40.2	25.7

^a $\tilde{\nu}_0^{\text{est}}$ and $\tilde{\nu}_\infty^{\text{SS}}$ are the peak frequencies of the estimated time-zero and the relaxed steady-state emission spectra and $\Delta\tilde{\nu}_{\text{est}}$ is the difference of the two. $\tilde{\nu}_0^{\text{FLUPS}}$, $\tilde{\nu}_\infty^{\text{FLUPS}}$, and $\Delta\tilde{\nu}_{\text{obs}}$ are the corresponding frequencies obtained from the global analysis of the FLUPS data. $\Delta\tilde{\nu}_{\text{dif}}$ is the difference between the observed and estimated total dynamic Stokes shift. ^b The solvation dynamics parameters were obtained from the global analysis of the FLUPS data. The average solvation times were calculated according to $\langle\tau\rangle = \sum \alpha_i \tau_i$. ^c Values from ESI, Table 1 of ref. 47.

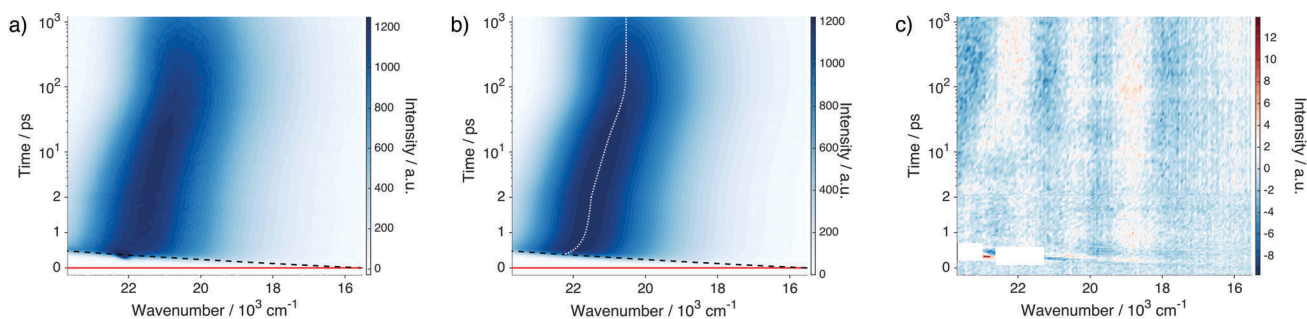


Fig. 3 (a) Time-resolved fluorescence of **C151** in EtOH; (b) best global fit ($\chi_r^2 = 2.30$); (c) weighted residual, all on a lin-log time axis. The dashed black line represents $t = 0$ estimated from the chirp correction and the dashed white line the peak maximum. The blank white areas seen in the residual are excluded from the fit and are due to Raman scattering. Excitation was at 400 nm.

The band-shape parameters of the time-resolved spectra were obtained using both the spectral and the global analyses. The spectral fits do not assume any time-dependent behavior of the parameters and can be considered as the best fits that can be achieved with the log-normal function. The time evolutions of the different parameters of all compounds in EtOH are presented in Fig. 4. The markers indicate the parameters obtained from the spectral analysis and serve as an additional guide to the eye in judging the goodness of the global fits. The lines represent the parameters from the global analysis assuming a constant or one to three exponential behavior depending on the sample and the parameter. The best-fit parameters of the peak frequencies are summarized

in Table 1. The remaining parameters are summarized in Table S1 (ESI[†]).

To investigate the probe dependence on the solvation dynamics in more detail, the time-resolved fluorescence of structurally similar compounds, **C151** and **4AP**, were additionally measured in PhCN and DMSO and analyzed using the global model. Since we were only interested in the solvation dynamics, the spectra were collected in a perpendicular polarization of the pump pulse relative to the gate pulse to reduce the signal from the Raman scattering and the spectra were further area-normalized prior to global analysis. However, due to multiple Raman peaks and large overlap with the emission spectra, the analysis in PhCN was carried out from $t \geq 160$ fs on the chirp corrected data. The spectra, best global fits,

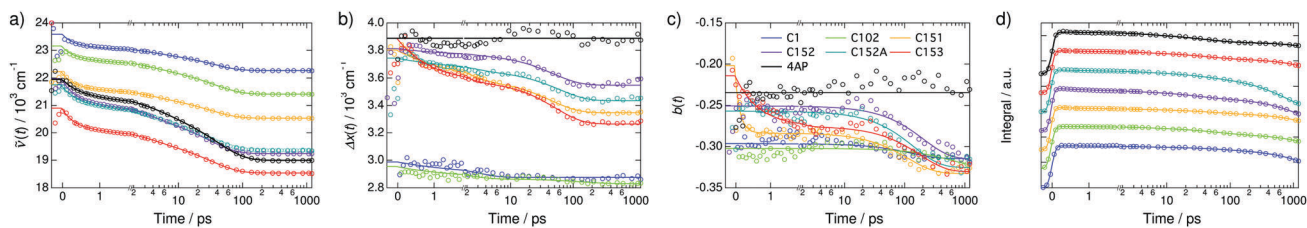


Fig. 4 Time evolution of the band-shape parameters of the fluorescence spectra in EtOH on a lin-log time axis: (a) peak position; (b) width parameter; (c) asymmetry parameter; and (d) band integral. The markers indicate the parameters obtained from the spectral analysis and serve as an additional guide to the eye in judging the goodness of the global fits. The lines represent the parameters obtained from the global analysis assuming a constant or one to three exponential behavior. The band integrals of different samples in (d) are vertically displaced for clarity.

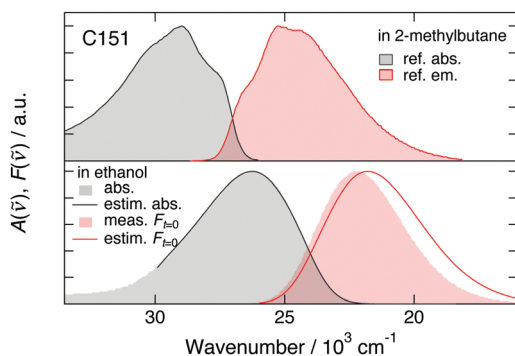


Fig. 5 Top panel: Absorption (gray) and emission (red) spectra of **C151** in 2MB used to estimate the time-zero spectra in EtOH. Bottom panel: Measured (gray fill) and estimated (black line) absorption spectra together with the measured (red fill) and estimated (red line) time-zero emission spectra of **151** in EtOH. The measured time-zero emission spectrum corresponds to the spectrum obtained from the global analysis of the FLUPS data at $t = 0$.

and residuals are shown in Fig. S2 and the parameters of the solvent relaxation are summarized in Table S2 (ESI[†]).

3.3 Estimation of the time-zero emission spectra

To estimate the accuracy of the time-zero emission spectra and the total dynamic Stokes shift obtained from the global analysis of the FLUPS data in EtOH, we determined both the spectra and the total shift using the steady-state method as described in the Experimental section.⁴⁶ The intrinsic band-shape functions were obtained from the absorption and emission spectra in nonpolar 2MB. Due to the negligible solubility of **4AP** in 2MB, we first prepared a saturated solution in dibutylether and transferred 10 μ l of this solution into 3 mL of 2MB. The residual dibutylether was found to have no influence on the position of the spectra. Representative spectra for **C151** are presented in Fig. 5. The other spectra are shown in Fig. S3 (ESI[†]). The parameters of the Gaussians (shift and width) are summarized in Table S3 (ESI[†]). The peak frequencies of the estimated time-zero emission spectra were obtained from fits of log-normal functions and are summarized in Table 1.

3.4 Fluorescence anisotropy decays

We measured the fluorescence anisotropy decays of the selected molecules, **C151** and **4AP**, in all three solvents, EtOH, PhCN, and DMSO. The aim was to test whether the rotational dynamics of the probe molecules play a role in the solvation dynamics as suggested in the literature.⁵⁷ The anisotropy decays were analyzed from $t \geq 50$ fs using multi-exponential functions (two to three). The normalized decays together with the best fits and residuals are shown in Fig. S5 and the best-fit parameters are summarized in Table S4 (ESI[†]). An example of a raw dataset of **4AP** in PhCN is shown in Fig. S6 (ESI[†]).

4 Discussion

4.1 Spectral parameters and total dynamic Stokes shift

Both the absorption and emission spectra show a clear trend in the series of coumarins. The band positions are red shifted

upon increasing electron donating strength of the amine substituent or upon increasing the electron withdrawing strength by using the trifluoromethyl substituent. The absorption spectra of the primary amine substituted compounds, **C151** and **4AP**, are significantly broader indicating the effect of hydrogen bonding. The broadening is less pronounced in the emission spectra which can be attributed to decreased hydrogen bonding in the excited state. This is expected due to the decrease of the electron density on the primary amine substituent in the excited state due to the push-pull nature of the compounds.

A similar effect is observed in the estimated spectra in EtOH.⁴⁶ The frequency shift of the spectra when going from nonpolar to polar solvent is significantly larger for **C151** and **4AP** due to the hydrogen bonding. Additionally, the broadening is significantly larger for **4AP** than for the coumarins. For all compounds, the estimated absorption spectra in polar solvents are nearly indistinguishable from the measured spectra (Fig. 5 and Fig. S3, ESI[†]).

To ensure that no ultrafast stage of solvation is missed in our FLUPS experiments, we compared the estimated time-zero emission spectra and the total dynamic Stokes shifts with those obtained from the global analysis of the FLUPS data. In most cases, the peak frequency of the observed time-zero spectrum is higher than that estimated from the steady-state spectra, the only exception being **C1**. The difference is largest for **C151** (Fig. 5) amounting to 460 cm^{-1} . However, the FLUPS data shows that the emission band of **C151** is significantly blue shifted from the estimated time-zero spectrum at early times as illustrated in Fig. 6. The peak frequency of the estimated time-zero spectrum coincides with the peak frequency of the measured emission at $t = 325$ fs. Therefore, the data clearly demonstrates that the

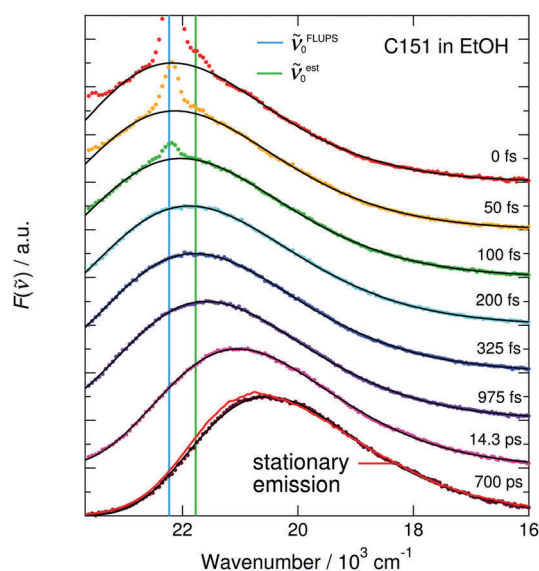


Fig. 6 Time evolution of the fluorescence of **C151** in EtOH. The markers indicate the data points and the black solid lines are the best-fits of log-normal functions. The observed (ν_0^{FLUPS}) and estimated (ν_0^{est}) time-zero peak frequencies are indicated by vertical blue and green lines, respectively. The stationary emission spectrum (red solid line) is overlaid with the time-resolved spectrum measured at 700 ps.

FLUPS is able to provide a more accurate description of the time-zero emission spectrum in this case. The same can be concluded for **C153** (Fig. S7, ESI†).

There are two possible reasons for the disagreement between the estimated and the observed time-zero spectra. First, the model used to estimate the spectra assumes emission from a vibrationally relaxed excited state and, in the case of excess excitation energy, contributions from higher vibronic states can influence the observed early-time emission. This is the case for **C153**, in particular, which has the largest amount of excess excitation energy. The observed time-zero spectrum is significantly broader than the estimated spectrum and narrows rapidly during the first few ps. Second, the model does not account for structural relaxation in the excited state. All six coumarins show significant deviations from mirror image symmetry between the absorption and emission transition dipole moment representation⁶⁸ (TDM) spectra in nonpolar 2MB (Fig. S4, ESI†) indicating non-negligible changes in the geometry in the excited state. The emission TDM spectra show a decreased intensity in the blue side compared to the absorption TDM spectra which results in an additional red shift of the estimated time-zero spectra in EtOH. Deviation from the mirror image symmetry is largest for **C151**⁵⁵ explaining the significantly larger disagreement in the time-zero spectra. **4AP**, on the other hand, exhibits nearly perfect mirror image symmetry and the agreement between the estimated and observed time-zero spectra is excellent ($\sim 50 \text{ cm}^{-1}$).

The situation is different for **C1**. In this case, the observed time-zero peak frequency is 360 cm^{-1} lower than the estimated frequency. The emission band at early times is at the limit of our detection window ($\tilde{\nu}_{\text{max}} = 23.6 \times 10^3 \text{ cm}^{-1}$) and the analysis in this region is further complicated by the Raman scattering. Hence the global analysis fails to accurately capture the short-time behavior and the frequency estimated from the steady-state spectra is considered more accurate.

Apart from **C1**, **C151**, and **C153** the agreement between the observed and estimated total dynamic Stokes shift is excellent ($\leq 100 \text{ cm}^{-1}$). This clearly demonstrates that all ultrafast solvation components are accurately captured by our measurements in EtOH with the exception of **C1**. The influence of the vibrational or structural relaxation in the case of **C153** and **C151** is discussed below.

4.2 Polar solvation dynamics in EtOH

The shifts of the peak frequencies of all compounds were analyzed assuming three-exponential behavior in the global model. Due to the definition of $C(t)$, eqn (1), the decay parameters of the peak positions are identical to those of the spectral relaxation function. As seen in Table 1, both the amplitudes and lifetimes are very similar among all measured coumarins with an average solvation time of *ca.* 17 ps. **C102** exhibits slightly slower solvent relaxation but the difference, in comparison to **C153**, is relatively small. Additionally, both the spectral and the dynamic parameters of **C153** are in very good agreement with those obtained more than 20 years ago by Maroncelli *et al.* using the spectral reconstruction method.⁴⁷

The similarity among the coumarins could easily result in the conclusion that the solvation dynamics are independent of the probe molecule.

Therefore, we additionally investigated **4AP**. The observed solvent relaxation of **4AP** is significantly slower than that of the coumarins. The amplitudes show less variation but all time constants are much larger resulting in a nearly 10 ps (or *ca.* 60%) longer average solvation time. This difference is significant and well above the uncertainty of the current measurements. The origin of this difference was further investigated in two additional solvents (see below).

4.3 Band-shape parameters and the effect of excess energy

The studied probe molecules with varying absorption maxima together with the fixed excitation wavelength enabled an investigation on the effect of excess energy. As discussed above, the excess energy does not have a significant influence on the solvation dynamics in agreement with earlier reports.^{47,69} The width and the asymmetry, on the other hand, show a clear trend among the studied dyes. As seen in Fig. 4(b) and (c) the width decreases and the asymmetry increases with time. The magnitudes of these changes are proportional to the amount of excess energy, being largest for **C153**, which exhibits a decrease of more than 600 cm^{-1} in the width parameter. The compounds with the least excess excitation energy, namely **C1**, **C102**, and **4AP**, exhibit nearly constant widths and asymmetries during the whole time evolution of the fluorescence. The fast changes can be attributed to intramolecular vibrational relaxation processes occurring during the first few ps which is clearly evident for **C153**. The fast dynamics of **C151** with only moderate amount of excess excitation energy, on the other hand, are rather attributed to the structural relaxation. This most likely involves rearrangement of the $-\text{NH}_2$ group but the nature of the changes is not clear. Further decrease in the bandwidth occurring on a much longer time scale ($\sim 50 \text{ ps}$) is observed for most coumarins and the amplitude correlates with the amount of excess excitation energy. This strongly suggests that the narrowing is related to vibrational cooling.⁷⁰

Similar changes in the band-shape parameters of push-pull probes were recently reported by Sajadi and Ernsting. Excitation with excess energy resulted in initial broadening within the time resolution of their experiment ($\sim 80 \text{ fs}$) followed by subsequent narrowing on a $\sim 10 \text{ ps}$ time scale. The initial fast processes, not fully detectable in our experiments, were attributed to intramolecular vibrational redistribution followed by cooling on a longer time scale.⁷¹

The last parameter to discuss is the band integral. In all cases the decays were clearly multi-exponential and were modeled using three-exponential functions convolved with a Gaussian simulated IRF (see Table S1, ESI†). The lifetimes of the major decay components agree surprisingly well with those measured using a ns-TCSPC considering the relatively short time window (1.2 ns) used in the FLUPS measurements and can be attributed to the decays of the excited-state populations. The two faster components, on the other hand, seem to correlate with the solvent relaxation. The lifetimes are similar to those of

the two slower solvation components, τ_2 and τ_3 in Table 1. Moreover, the total amplitude of these components somewhat correlate with the magnitude of the total dynamic Stokes shift, being largest for **4AP** (25%) and **C152** (23%). This demonstrates that the multi-exponential decay of the band integral partially originates from the decrease of the radiative rate, which depends on the frequency *via* $\tilde{\nu}^3$, as also discussed in the literature.^{47,53,72}

To test this, we divided the time-resolved fluorescence data by $\tilde{\nu}^3$ and reanalyzed it using the global model (results not shown). The results are not discussed in detail but a few observations are worth mentioning. First of all, all best-fit parameters change to some extent but the solvation dynamics are not significantly altered. The spectra are broader and the asymmetry is larger as expected. Interestingly, the decay integrals are still multi-exponential (two to three) but the faster components exhibit negative amplitudes amounting to a rise of ~ 10 –15% in the emission integral. This indicates that the transition dipole moment actually increases during solvent relaxation. This is also predicted by recent theoretical models involving two coupled states, a neutral state and a charge-transfer state.^{73,74} For a more thorough discussion about the different models see ref. 75 and the references therein. The band integral can, of course, be additionally influenced by other relaxation phenomena (structural or vibrational) but a detailed discussion is beyond the scope of the present manuscript.

4.4 Probe dependence

As discussed above, the solvation dynamics between the coumarins and **4AP** were significantly different in EtOH. The differences could result from specific solute–solvent interactions. Hence we chose two additional solvents, DMSO and PhCN, to investigate the probe dependence in detail for two selected compounds, **C151** and **4AP**, both bearing a primary amine substituent. DMSO is a good hydrogen-bond acceptor whereas PhCN is a relatively weakly interacting solvent. The spectral relaxation functions in all three solvents are depicted in Fig. 7.

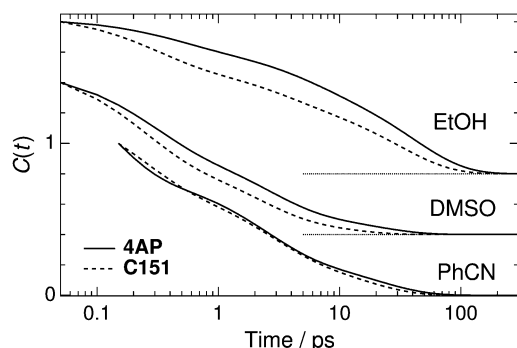


Fig. 7 Spectral relaxation functions of **4AP** (solid line) and **C151** (dashed line) in EtOH, DMSO, and PhCN. All functions were obtained from the global analysis of the FLUPS data. The data in EtOH and DMSO are normalized at $t = 50$ fs and in PhCN at $t = 160$ fs due to the limited fitting range. The relaxation functions in different solvents are vertically displaced by 0.4 for clarity.

Similar to EtOH, the solvent relaxation of **4AP** in DMSO is significantly slower compared to that of **C151** whereas in PhCN the relaxation is nearly identical. This clearly points to specific solute–solvent interactions. Both compounds are able to both donate and accept hydrogen bonds and the significant deceleration of the solvent relaxation of **4AP** indicates significantly stronger hydrogen-bonding interactions. The solvation dynamics of **C151**, on the other hand, are very similar to those of **C153** in all three solvents (Table S2, ESI†).⁴⁷ This suggests that the specific solute–solvent interactions are comparable for the two compounds and the primary amine group of **C151** does not significantly influence the solvent relaxation. Most likely the hydrogen bonds donated by the $-\text{NH}_2$ group are cleaved in the excited state. Based on the relatively slower solvent relaxation, this is not the case for **4AP**.

Last, we wanted to explore the possible effect of the rotational diffusion of the solute on the solvation dynamics. The normalized spectral relaxation functions together with the fluorescence anisotropy decays of **C151** and **4AP** in all three solvents are presented in Fig. S8 (ESI†). In all solvents, the anisotropy decays are significantly slower than the solvent relaxation functions. In addition, we were not able to reproduce the solvent relaxation of the faster probe by accounting for the rotational diffusion using the method proposed in the literature.⁵⁷ It is, however, clear that specific interactions influence the rotational relaxation. Deviations of the average rotational relaxation times from simple hydrodynamic theory seem to correlate with the degree of specific interactions and the deceleration of the solvent relaxation (see Table S5 and related discussion, ESI†). These two processes, however, occur on significantly different time scales. For example, the solvent relaxation in DMSO has an average lifetime of ~ 2 –4 ps whereas the rotational relaxation occurs on a ~ 100 –200 ps time scale. Hence the model proposed in the literature appears to be oversimplified and cannot account for the differences observed in the solvation dynamics of the present study.

4.5 Spectral vs. global analysis

Finally, we want to outline the major advantages of the global analysis over the spectral analysis. The first and most obvious advantage is the greatly reduced number of fitting parameters. The dataset presented in Fig. 3 consists of 140 time-steps and *ca.* 25 000 data points. In the global analysis, the full dataset is analyzed with 25 adjustable parameters and the final results presented in Fig. 4 are directly obtained. We want to emphasize that we did not use any constraints in the fits. Spectral analysis of the same dataset would require four log-normal parameters for each time delay amounting to a total of 560 adjustable parameters after which the obtained band-shape parameters would be further analyzed with exponential functions. The second major advantage is the analysis of the early-time behavior. The implementation of the independently estimated chirp polynomial and the convolution of the decay behavior with the Gaussian simulated IRF significantly increases the accuracy of the fit around $t = 0$ and the time-zero spectra are directly obtained from the global analysis.

The quality of the fits in both approaches is good and the deviation from $\chi_r^2 = 1$ can be mostly attributed to an inadequate

description of the emission band-shape by the log-normal function. This is also seen in the residuals at longer times ($t > 1$ ps). However, the χ_r^2 values from the spectral analysis are significantly better which is attributed to the quality of the fit around $t = 0$, also visible in the residual presented in Fig. 3(c). Due to the high density of points around $t = 0$ small deviations between the model and the fit contribute significantly to the calculated χ_r^2 value. For example, χ_r^2 values from the spectral/global analysis for **C151** are 1.71/2.30 in EtOH (fit from $t < 0$) and 2.77/2.85 in PhCN (fit from $t \geq 160$ fs). In the spectral analysis, the band-shape parameters are freely adjustable resulting in “nonphysical” values around $t = 0$, thus improving the fit quality. This is avoided in the global analysis and it produces more reliable values especially in cases where the peak frequency around $t = 0$ is overlapped with the Raman scattering or is close to the edge of the detection window *e.g.* for **C1** and **C102**. The remaining patterns in the residual around $t = 0$ could be partially due to inadequate removal of the Raman signal or due to an inaccurate description of the chirp. However, including the coefficients of the chirp polynomial as fitting parameters did not improve the fit quality. Additionally, ultrafast dynamics not accounted for in the fitting model can contribute to the residuals.

The last major advantage of the global analysis is the possibility to combine it with target analysis. In this case, one would use two or more band-shape functions, each corresponding to a separate chemical species, connected *via* rate equations. All species can be allowed to undergo solvent relaxation and the population dynamics can be independently accessed through the band integrals which is not possible in conventional global lifetime analysis.^{62,76–79} In our approach, contributions from the solvent relaxation and the population dynamics are clearly separated even if they occur on a similar time scale. Surprisingly, this approach has not yet been exploited in the literature and work in this direction is currently underway in our laboratory.

5 Conclusions

We have investigated the polar solvation dynamics of seven push–pull probes in ethanol using a novel global analysis of broadband fluorescence data. Fits are performed from $t < 0$ and the time-zero emission spectra are directly obtained. These spectra are demonstrated to be of high accuracy and agree well with those estimated from the steady-state spectra in the absence of significant structural or vibrational relaxation. The spectral relaxation functions of the coumarins are similar but distinctly different from that of 4-aminophthalimide. The differences are attributed to specific solute–solvent interactions. This conclusion is further corroborated by comparing the solvation dynamics of two compounds, **C151** and **4AP**, in DMSO and PhCN. In strongly interacting DMSO, **4AP** exhibits a *ca.* twofold slower solvent relaxation than **C151** whereas in weakly interacting PhCN the dynamics are nearly identical. The specific solute–solvent interactions are also observed in the rotational dynamics as deviations from a simple hydrodynamic theory.

Our results clearly demonstrate the molecularity of solvation *i.e.* solvation dynamics in interacting solvents are dependent on the probe molecule. This, however, is not in violation with the linear response approximation.

Second, we have investigated the effect of excess excitation energy on the solvent relaxation and the time-dependent band-shape parameters of the fluorescence in EtOH. The excess excitation energy is found to have no influence on the solvation dynamics, whereas it results in significant time-dependent narrowing and increase in the asymmetry of the fluorescence band. The fast changes occurring during the first few ps are ascribed to structural and intramolecular vibrational relaxation processes whereas further narrowing on a longer time scale probably originates from vibrational cooling to the solvent bath. In the case of negligible excess energy, the width and the asymmetry remain constant.

The global analysis described in this work represents the first example where a full fs broadband fluorescence dataset is analyzed within a single model simultaneously accounting for the chirp and the convolution with a finite excitation pulse. This type of analysis is customary for fs transient absorption data and in our opinion is a natural extension for the broadband fluorescence technique. When combined with a target analysis, such a model can be used for investigations of various excited-state processes such as electron- or proton-transfer reactions where the solvation must be explicitly accounted for. The model gives direct access to the intrinsic population dynamics and simplifies further testing of different kinetic models.

Acknowledgements

We wish to thank Prof. N. P. Ernsting for his help with the FLUPS setup and acknowledge financial support from the Fonds National Suisse de la Recherche Scientifique through project No. 200020-165890 and the University of Geneva.

References

- 1 L. D. Zusman, *Chem. Phys.*, 1980, **49**, 295–304.
- 2 I. Rips and J. Jortner, *J. Chem. Phys.*, 1987, **87**, 2090–2104.
- 3 I. Rips and J. Jortner, *J. Chem. Phys.*, 1988, **88**, 818–822.
- 4 E. M. Kosower and D. Huppert, *Chem. Phys. Lett.*, 1983, **96**, 433–435.
- 5 T. J. Kang, W. Jarzeba, P. F. Barbara and T. Fonseca, *Chem. Phys.*, 1990, **149**, 81–95.
- 6 K. Tominaga, G. C. Walker, W. Jarzeba and P. F. Barbara, *J. Phys. Chem.*, 1991, **95**, 10475–10485.
- 7 M. L. Horng, K. Dahl, G. Jones II and M. Maroncelli, *Chem. Phys. Lett.*, 1999, **315**, 363–370.
- 8 N. Banerji, G. Angulo, I. Barabanov and E. Vauthey, *J. Phys. Chem. A*, 2008, **112**, 9665–9674.
- 9 X. Li and M. Maroncelli, *J. Phys. Chem. A*, 2011, **115**, 3746–3754.

- 10 P. M. Kiefer and J. T. Hynes, *J. Phys. Chem. A*, 2002, **106**, 1834–1849.
- 11 P.-T. Chou, S.-C. Pu, Y.-M. Cheng, W.-S. Yu, Y.-C. Yu, F.-T. Hung and W.-P. Hu, *J. Phys. Chem. A*, 2005, **109**, 3777–3787.
- 12 Y.-M. Cheng, S.-C. Pu, C.-J. Hsu, C.-H. Lai and P.-T. Chou, *ChemPhysChem*, 2006, **7**, 1372–1381.
- 13 J. L. Pérez-Lustres, F. Rodríguez-Prieto, M. Mosquera, T. A. Senyushkina, N. P. Ernsting and S. A. Kovalenko, *J. Am. Chem. Soc.*, 2007, **129**, 5408–5418.
- 14 Y. Kimura, M. Fukuda, K. Suda and M. Terazima, *J. Phys. Chem. B*, 2010, **114**, 11847–11858.
- 15 K. Suda, M. Terazima and H. Sato, *J. Phys. Chem. B*, 2013, **117**, 12567–12582.
- 16 B. Bagchi, *Annu. Rev. Phys. Chem.*, 1989, **40**, 115–141.
- 17 P. F. Barbara, G. C. Walker and T. P. Smith, *Science*, 1992, **256**, 975–981.
- 18 F. O. Raineri and H. L. Friedman, *Adv. Chem. Phys.*, 1999, **107**, 81–189.
- 19 C.-C. Hsieh, C.-M. Jiang and P.-T. Chou, *Acc. Chem. Res.*, 2010, **43**, 1364–1374.
- 20 A. P. Demchenko, K.-C. Tang and P.-T. Chou, *Chem. Soc. Rev.*, 2013, **42**, 1379–1408.
- 21 T. Kumpulainen, B. Lang, A. Rosspeintner and E. Vauthey, *Chem. Rev.*, 2016, DOI: 10.1021/acs.chemrev.6b00491.
- 22 A. V. Benderskii and K. B. Eisenthal, *J. Phys. Chem. A*, 2002, **106**, 7482–7490.
- 23 A. Paul and A. Samanta, *J. Phys. Chem. B*, 2007, **111**, 4724–4731.
- 24 A. Samanta, *J. Phys. Chem. Lett.*, 2010, **1**, 1557–1562.
- 25 S. K. Pal, L. Zhao and A. H. Zewail, *Proc. Natl. Acad. Sci. U. S. A.*, 2003, **100**, 8113–8118.
- 26 S. K. Pal and A. H. Zewail, *Chem. Rev.*, 2004, **104**, 2099–2123.
- 27 B. Bagchi, *Chem. Rev.*, 2005, **105**, 3197–3219.
- 28 D. Andreatta, J. L. Pérez Lustres, S. A. Kovalenko, N. P. Ernsting, C. J. Murphy, R. S. Coleman and M. A. Berg, *J. Am. Chem. Soc.*, 2005, **127**, 7270–7271.
- 29 D. Andreatta, S. Sen, J. L. Pérez Lustres, S. A. Kovalenko, N. P. Ernsting, C. J. Murphy, R. S. Coleman and M. A. Berg, *J. Am. Chem. Soc.*, 2006, **128**, 6885–6892.
- 30 A. Fürstenberg, O. Kel, J. Gradinaru, T. R. Ward, D. Emery, G. Bollot, J. Mareda and E. Vauthey, *ChemPhysChem*, 2009, **10**, 1517–1532.
- 31 Y. Yang, Y. Qin, Q. Ding, M. Bakhtina, L. Wang, M.-D. Tsai and D. Zhong, *Biochemistry*, 2014, **53**, 5405–5413.
- 32 C. P. Hsu, X. Y. Song and R. A. Marcus, *J. Phys. Chem. B*, 1997, **101**, 2546–2551.
- 33 E. W. Castner, Jr and M. Maroncelli, *J. Mol. Liq.*, 1998, **77**, 1–36.
- 34 W. P. de Boeij, M. S. Pshenichnikov and D. A. Wiersma, *Annu. Rev. Phys. Chem.*, 1998, **49**, 99–123.
- 35 D. A. Turton, J. Hunger, A. Stoppa, G. Hefter, A. Thoman, M. Walther, R. Buchner and K. Wynne, *J. Am. Chem. Soc.*, 2009, **131**, 11140–11146.
- 36 M. Maroncelli, *J. Mol. Liq.*, 1993, **57**, 1–37.
- 37 M. Glasbeek and H. Zhang, *Chem. Rev.*, 2004, **104**, 1929–1954.
- 38 B. Bagchi and B. Jana, *Chem. Soc. Rev.*, 2010, **39**, 1936–1954.
- 39 B. Bagchi, D. W. Oxtoby and G. R. Fleming, *Chem. Phys.*, 1984, **86**, 257–267.
- 40 M. Maroncelli and G. R. Fleming, *J. Chem. Phys.*, 1987, **86**, 6221–6239.
- 41 J. H. Easter, R. P. DeToma and L. Brand, *Biophys. J.*, 1976, **16**, 571–583.
- 42 R. D. B. Fraser and E. Suzuki, *Anal. Chem.*, 1969, **41**, 37–39.
- 43 P. F. Rusch and J. P. Lelieur, *Anal. Chem.*, 1973, **45**, 1541–1543.
- 44 S. J. Rosenthal, X. Xie, M. Du and G. R. Fleming, *J. Chem. Phys.*, 1991, **95**, 4715–4718.
- 45 I. Eom and T. Joo, *J. Chem. Phys.*, 2009, **131**, 244507.
- 46 R. S. Fee and M. Maroncelli, *Chem. Phys.*, 1994, **183**, 235–247.
- 47 M. L. Horng, J. A. Gardecki, A. Papazyan and M. Maroncelli, *J. Phys. Chem.*, 1995, **99**, 17311–17337.
- 48 L. Zhao, J. L. Pérez-Lustres, V. Farztdinov and N. P. Ernsting, *Phys. Chem. Chem. Phys.*, 2005, **7**, 1716–1725.
- 49 X.-X. Zhang, C. Würth, L. Zhao, U. Resch-Genger, N. P. Ernsting and M. Sajadi, *Rev. Sci. Instrum.*, 2011, **82**, 063108.
- 50 M. Gerecke, G. Bierhance, M. Gutmann, N. P. Ernsting and A. Rosspeintner, *Rev. Sci. Instrum.*, 2016, **87**, 053115.
- 51 M. A. Kahlou, T. J. Kang and P. F. Barbara, *J. Chem. Phys.*, 1988, **88**, 2372–2378.
- 52 S. G. Su and J. D. Simon, *J. Phys. Chem.*, 1989, **93**, 753–758.
- 53 W. Jarzaba, G. C. Walker, A. E. Johnson and P. F. Barbara, *Chem. Phys.*, 1991, **152**, 57–68.
- 54 C. F. Chapman, R. S. Fee and M. Maroncelli, *J. Phys. Chem.*, 1995, **99**, 4811–4819.
- 55 T. Gustavsson, L. Cassara, V. Gulbinas, G. Gurzadyan, J. C. Mialocq, S. Pommeret, M. Sorgius and P. van der Meulen, *J. Phys. Chem. A*, 1998, **102**, 4229–4245.
- 56 N. Ito, S. Arzhantsev and M. Maroncelli, *Chem. Phys. Lett.*, 2004, **396**, 83–91.
- 57 M. Sajadi, M. Weinberger, H.-A. Wagenknecht and N. P. Ernsting, *Phys. Chem. Chem. Phys.*, 2011, **13**, 17768–17774.
- 58 X.-X. Zhang, J. Breffke, N. P. Ernsting and M. Maroncelli, *Phys. Chem. Chem. Phys.*, 2015, **17**, 12949–12956.
- 59 R. A. Marcus, *J. Chem. Phys.*, 1965, **43**, 679–701.
- 60 R. Cammi and B. Mennucci, *J. Chem. Phys.*, 1999, **110**, 9877–9886.
- 61 J. L. Pérez-Lustres, S. A. Kovalenko, M. Mosquera, T. Senyushkina, W. Flasche and N. P. Ernsting, *Angew. Chem., Int. Ed.*, 2005, **44**, 5635–5639.
- 62 C. Slavov, H. Hartmann and J. Wachtveitl, *Anal. Chem.*, 2015, **87**, 2328–2336.
- 63 J. A. Gardecki and M. Maroncelli, *Appl. Spectrosc.*, 1998, **52**, 1179–1189.
- 64 P.-A. Muller, C. Högemann, X. Allonas, P. Jacques and E. Vauthey, *Chem. Phys. Lett.*, 2000, **326**, 321–327.
- 65 A. Morandeira, L. Engeli and E. Vauthey, *J. Phys. Chem. A*, 2002, **106**, 4833–4837.
- 66 G. Duvanel, J. Grilj, H. Chaumeil, P. Jacques and E. Vauthey, *Photochem. Photobiol. Sci.*, 2010, **9**, 908–915.
- 67 E. Tokunaga, A. Terasaki and T. Kobayashi, *J. Opt. Soc. Am. B*, 1996, **13**, 496–513.

- 68 G. Angulo, G. Grampp and A. Rosspeintner, *Spectrochim. Acta, Part A*, 2006, **65**, 727–731.
- 69 L. Reynolds, J. A. Gardecki, S. J. V. Frankland, M. L. Horng and M. Maroncelli, *J. Phys. Chem.*, 1996, **100**, 10337–10354.
- 70 A. Pigliucci, G. Duvanel, L. M. L. Daku and E. Vauthey, *J. Phys. Chem. A*, 2007, **111**, 6135–6145.
- 71 M. Sajadi and N. P. Ernsting, *J. Phys. Chem. B*, 2013, **117**, 7675–7684.
- 72 M. Maroncelli, R. S. Fee, C. F. Chapman and G. R. Fleming, *J. Phys. Chem.*, 1991, **95**, 1012–1014.
- 73 D. V. Matyushov and M. D. Newton, *J. Phys. Chem. A*, 2001, **105**, 8516–8532.
- 74 A. Painelli and F. Terenziani, *J. Phys. Chem. A*, 2000, **104**, 11041–11048.
- 75 S. Arzhantsev, K. A. Zachariasse and M. Maroncelli, *J. Phys. Chem. A*, 2006, **110**, 3454–3470.
- 76 R. Bonneau, J. Wirz and A. D. Zuberbuhler, *Pure Appl. Chem.*, 1997, **69**, 979–992.
- 77 I. H. M. van Stokkum, D. S. Larsen and R. van Grondelle, *Biochim. Biophys. Acta, Bioenerg.*, 2004, **1657**, 82–104.
- 78 J. Snellenburg, S. Liptonok, R. Seger, K. Mullen and I. Van Stokkum, *J. Stat. Softw.*, 2012, **49**, 1–22.
- 79 L. J. G. W. van Wilderen, C. N. Lincoln and J. J. van Thor, *PLoS One*, 2011, **6**, e17373.